6th European Conference on Computational Mechanics (ECCM 6)
7th European Conference on Computational Fluid Dynamics (ECFD 7)
11–15 June 2018, Glasgow, UK

IMMERSED BOUNDARY FINITE ELEMENT HYPERELASTIC HEART MODEL

CHARLES PUELZ[1], MARGARET ANNE SMITH[1], SIMONE ROSSI[1], GREG STURGEON[2], PAUL SEGARS[2] AND BOYCE E. GRIFFITH[1]

[1]Department of Mathematics
University of North Carolina, Chapel Hill
120 E Cameron Avenue, CB #3250
329 Phillips Hall, Chapel Hill, NC 27599

[2]Department of Radiology
Duke University School of Medicine
Box 3808 DUMC
Durham, NC 27710

Key words: Fluid–Structure Interaction, Immersed Boundary Method, Hyperelastic Models, Cardiovascular Models.

Abstract. In this work, we describe a computational model of the human heart incorporating the great vessels and the four valves. The heart and vessel geometries are segmented from computed tomography data; heart valves are represented by idealized geometrical models. The heart tissue is modeled as a viscoelastic material: the hyperelastic transversely isotropic Guccione's constitutive law is used to describe the elastic behavior of the heart wall, while the viscosity is inherited from a permeating viscous fluid. The anisotropy fields are determined using Poisson interpolation techniques to qualitatively match anatomical muscle bundles so that the fiber vector field corresponds to the orientation of the cardiomyocytes. Realistic models for the aorta and pulmonary artery, modeled as viscoelastic neo–Hookean materials, provide physiological outflow geometries for the left and right sides of the heart respectively. Fluid-structure interaction is performed via immersed–boundary spreading and restriction operators. Therefore, the solid model for the heart is immersed in a fluid model for the blood. We assume that the blood can be described by the incompressible Navier–Stokes equations. A Lagrangian finite element approximation is used for the solid mechanics, while a finite difference MAC scheme is employed for discretizing the fluid equations.

1 INTRODUCTION

In this paper, we describe some preliminary efforts in the development of a computer model of the human heart which includes the four chambers, valves, pulmonary artery, and ascending aorta. This model employs a hyperelastic description of the heart and its components, which are immersed in blood described by the incompressible Navier Stokes

equations. Our computational approach treats the fluid–structure interaction with the immersed boundary method, with the solid displacement described in Lagrangian form on a finite element mesh and the fluid pressure and velocity represented in Eulerian form on a fixed Cartesian grid.

Other models for the entire heart, or its components, have been put forth in the literature. We highlight several contributions, although this review is far from complete. Peskin and McQueen developed one of the first fluid–structure interaction models of a four chamber heart [9]. Structures in their model were represented as a collection of one dimensional fibers, constructed with careful consideration of physiological muscle fiber orientation. An extension of this approach to a model derived from computed tomography (CT) data of a human heart can be found in [10]. Another model from Baillargeon et al. considers only the heart myocardium, great vessels, and valves, without a model for the fluid [1]. Their approach instead couples hyperelastic solid mechanics of the myocardium to a description of the electrophysiology. Lastly, the University of Tokyo heart simulator describes the blood, the heart structure, and the electrophysiology using the Arbitrary Lagrangian Eulerian approach for fluid–solid coupling and homogenization to account for the electrical dynamics [13, 12].

Recent research has also focused on refining models for certain parts of the cardiac anatomy. Efforts related to electrophysiology, cardiac solid mechanics, and fluid–structure interaction can be found in the review by Quarteroni et al. [11]. Gao et al. recently assembled an immersed boundary model for the left heart, including the mitral valve and aortic outflow tract, which captures some complex valvular dynamics [5]. We also mention the work of Hirschvogel et al. in which they couple a biventricular solid mechanics model to a reduced description the peripheral circulation [7].

To our knowledge, the work presented here is one of the first whole heart models with a volumetric solid mechanical description of the valves, myocardium, and great vessels which employs an immersed boundary approximation for the fluid–structure interaction. This approach enables us to easily deal with large deformations during active contraction, and more readily define various fiber–reinforced constitutive models for the myocardium.

2 MATHEMATICAL MODELS

Immersed boundary methods rely on an Eulerian description of the fluid and a Lagrangian description of the solid. Our presentation follows [4]. The Eulerian coordinate domain is $\Omega \subset \mathbb{R}^3$ with $\boldsymbol{x} \in \Omega$ denoting an Eulerian coordinate. The set U denotes the Lagrangian coordinate domain with $\boldsymbol{X} \in U$ a material point of the solid.

For a given time t, the motion map $\boldsymbol{\chi}(\cdot, t) : U \to \Omega$ relates Lagrangian points with their corresponding Eulerian points. For example, at time t, the Eulerian point $\boldsymbol{\chi}(\boldsymbol{X}, t) \in \Omega$ corresponds to the material point $\boldsymbol{X}$. The deformation gradient and its determinant are defined as $\mathbb{F} = \frac{\partial \boldsymbol{\chi}}{\partial \boldsymbol{X}}, \quad J = \det(\mathbb{F})$. Mathematical models for the fluid and solid are given in terms of the total Cauchy stress:

$$\boldsymbol{\sigma}(\boldsymbol{x}, t) = \boldsymbol{\sigma}^{\mathrm{f}}(\boldsymbol{x}, t) + \begin{cases} \boldsymbol{\sigma}^{\mathrm{s}}(\boldsymbol{x}, t) & \text{if } \boldsymbol{x} \in \boldsymbol{\chi}(U, t) \\ \mathbf{0} & \text{otherwise.} \end{cases}$$

The tensor $\boldsymbol{\sigma}^{\mathrm{f}}$ corresponds to a viscous incompressible fluid defined in terms of the Eulerian velocity field $\boldsymbol{u}$, the pressure p, and the dynamic viscosity μ as follows

$$\boldsymbol{\sigma}^{\mathrm{f}}(\boldsymbol{x},t) = -p\boldsymbol{I} + \mu\left(\nabla\boldsymbol{u} + \nabla\boldsymbol{u}^T\right).$$

Assuming a hyperelastic model can be used to describe the elastic behavior of the solid tissue, the solid stress is derived from a pseudo–strain energy functional $\mathcal{W} = \mathcal{W}(\mathbb{F})$. Additionally, we assume that the strain-energy can be decomposed as $\mathcal{W} = W(\mathbb{F}) + U(J)$, where $W(\mathbb{F})$ characterizes the isochoric deformations, while $U(J)$ penalizes changes in volume. Define the first Piola–Kirchoff stress as

$$\mathbb{P}^{\mathrm{s}} = \mathrm{DEV}\left[\frac{\partial W}{\partial \mathbb{F}}\right] + JU'(J)\mathbb{F}^{-T},$$

where the operator $\mathrm{DEV}\left[\bullet\right] = (\bullet) - \frac{1}{3}(\bullet : \mathbb{F})\,\mathbb{F}^{-T}$. The elastic part of the Cauchy stress for the solid $\boldsymbol{\sigma}^s$ can be found using the transformation

$$\boldsymbol{\sigma}^{\mathrm{s}} = J^{-1}\mathbb{P}^{\mathrm{s}}\mathbb{F}^T.$$

In this formulation the fluid and solid stresses are superimposed in the evolving solid region $\boldsymbol{\chi}(U,t)$. This choice endows the solid with a viscoelastic response from the background fluid. Denoting with ρ the fluid density, the strong form for the equations of motion, as derived by Boffi et al. [2], read

$$\rho\left(\frac{\partial \boldsymbol{u}}{\partial t}(\boldsymbol{x},t) + \boldsymbol{u}(\boldsymbol{x},t)\cdot\nabla\boldsymbol{u}(\boldsymbol{x},t)\right) = -\nabla p(\boldsymbol{x},t) + \mu\Delta\boldsymbol{u}(\boldsymbol{x},t) + \boldsymbol{f}(\boldsymbol{x},t) + \boldsymbol{f}_{\mathrm{ext}}(\boldsymbol{x},t), \quad (1)$$

$$\nabla\cdot\boldsymbol{u}(\boldsymbol{x},t) = 0, \quad (2)$$

$$\boldsymbol{f}(\boldsymbol{x},t) = \int_U \nabla_{\boldsymbol{X}}\cdot\mathbb{P}^{\mathrm{s}}(\boldsymbol{X},t)\,\delta(\boldsymbol{x}-\boldsymbol{\chi}(\boldsymbol{X},t))d\boldsymbol{X} - \int_{\partial U}\mathbb{P}^{\mathrm{s}}(\boldsymbol{X},t)\boldsymbol{N}(\boldsymbol{X})\,\delta(\boldsymbol{x}-\boldsymbol{\chi}(\boldsymbol{X},t))dA(\boldsymbol{X}), \quad (3)$$

$$\boldsymbol{f}_{\mathrm{ext}}(\boldsymbol{x},t) = \int_U \boldsymbol{F}_{\mathrm{bdy}}(\boldsymbol{X},t)\,\delta(\boldsymbol{x}-\boldsymbol{\chi}(\boldsymbol{X},t))d\boldsymbol{X} + \int_{\partial U}\boldsymbol{F}_{\mathrm{surf}}(\boldsymbol{X},t)\,\delta(\boldsymbol{x}-\boldsymbol{\chi}(\boldsymbol{X},t))dA(\boldsymbol{X}), \quad (4)$$

$$\frac{\partial\boldsymbol{\chi}}{\partial t}(\boldsymbol{X},t) = \int_\Omega \boldsymbol{u}(\boldsymbol{x},t)\,\delta(\boldsymbol{x}-\boldsymbol{\chi}(\boldsymbol{X},t))d\boldsymbol{X}. \quad (5)$$

Equation (1) describes balance of momentum, where $\boldsymbol{f}$ incorporates the stress of the solid and $\boldsymbol{f}_{\mathrm{ext}}$ the external surface forces $\boldsymbol{F}_{\mathrm{surf}}$ and body forces $\boldsymbol{F}_{\mathrm{bdy}}$. The solid imparts both volumetric and surface force densities $\nabla_{\boldsymbol{X}}\cdot\mathbb{P}^{\mathrm{s}}$ and $-\mathbb{P}^{\mathrm{s}}\boldsymbol{N}$ on the fluid, which are spread onto the fluid via delta function kernels. Equation (2) enforces incompressibility in both the fluid and solid regions, and equation (5) requires the solid to move with the same velocity as the background fluid.

3 COMPUTATIONAL METHODS

The fluid equations are discretized with a Marker and Cell scheme on a fixed Cartesian grid, where the pressure is represented as a cell–centered variable and the velocity is represented at the sides of the cell. The motion of the solid is approximated with a C^0 finite element method in its reference configuration. In particular, the volumetric and surface force densities are projected onto a finite element basis by seeking $\boldsymbol{G}(\boldsymbol{X},t)$ so that

$$\begin{aligned}\int_U \boldsymbol{G}(\boldsymbol{X},t)\cdot\boldsymbol{V}_h(\boldsymbol{X})\,d\boldsymbol{X} = &-\int_U \mathbb{P}^{\mathrm{s}}(\boldsymbol{X},t):\nabla_{\boldsymbol{X}}\boldsymbol{V}_h(\boldsymbol{X})\,d\boldsymbol{X}\\ &+\int_U \boldsymbol{F}_{\mathrm{bdy}}(\boldsymbol{X},t)\cdot\boldsymbol{V}_h(\boldsymbol{X})\,d\boldsymbol{X}+\int_{\partial U}\boldsymbol{F}_{\mathrm{surf}}(\boldsymbol{X},t)\cdot\boldsymbol{V}_h(\boldsymbol{X})\,dA(\boldsymbol{X})\end{aligned}\tag{6}$$

for all $\boldsymbol{V}_h(\boldsymbol{X})$. This approximation to the force density is spread onto the fluid with a delta function kernel:

$$\boldsymbol{g}(\boldsymbol{x},t)=\int_U \boldsymbol{G}(\boldsymbol{X},t)\delta(\boldsymbol{x}-\boldsymbol{\chi}(\boldsymbol{X},t))d\boldsymbol{X}=\mathcal{S}\left[\boldsymbol{G}(\boldsymbol{X},t)\right],$$

where we call $\mathcal{S}$ the spreading operator. The adjoint of the spreading operator, denoted $\mathcal{J}$ and called the restriction operator, is used to impose the no slip condition between the fluid and solid. The equations of motion are then approximated by the following unified weak formulation:

$$\rho\left(\frac{\partial\boldsymbol{u}}{\partial t}(\boldsymbol{x},t)+\boldsymbol{u}(\boldsymbol{x},t)\cdot\nabla\boldsymbol{u}(\boldsymbol{x},t)\right)=-\nabla p(\boldsymbol{x},t)+\mu\Delta\boldsymbol{u}(\boldsymbol{x},t)+\boldsymbol{g}(\boldsymbol{x},t),\tag{7}$$

$$\nabla\cdot\boldsymbol{u}(\boldsymbol{x},t)=0,\tag{8}$$

$$\boldsymbol{g}(\boldsymbol{x},t)=\mathcal{S}\left[\boldsymbol{G}(\boldsymbol{X},t)\right],\tag{9}$$

$$\frac{\partial\boldsymbol{\chi}}{\partial t}(\boldsymbol{X},t)=\mathcal{J}\left[\boldsymbol{u}(\boldsymbol{x},t)\right].\tag{10}$$

To discretize the Lagrangian–Eulerian interaction encoded in the spreading and restriction operators $\mathcal{S}$ and $\mathcal{J}$, an approximation $\mathcal{S}_h$ is first constructed from a discretized delta function kernel. Then, the discrete adjoint of $\mathcal{S}_h$ is used for $\mathcal{J}$, ensuring energy conservation at the discrete level. For more details about numerical methods and timestepping, please refer to [4]. Our simulations use the IBAMR[1] software infrastructure.

4 MODEL CONSTRUCTION

The image data for this model consists of computed tomography (CT) scans of a normal adult human heart obtained from Duke University Medical Center, with resolution $256\times156\times186$. A dual source Siemens scanner was used for data acquisition. The slice thickness is 0.8 mm and the XY resolution is 0.644 mm.

A hexahedral mesh for the four heart chambers was initially constructed from this data. The aorta and pulmonary artery were separately segmented using ITK-SNAP. Our

[1] https://ibamr.github.io/

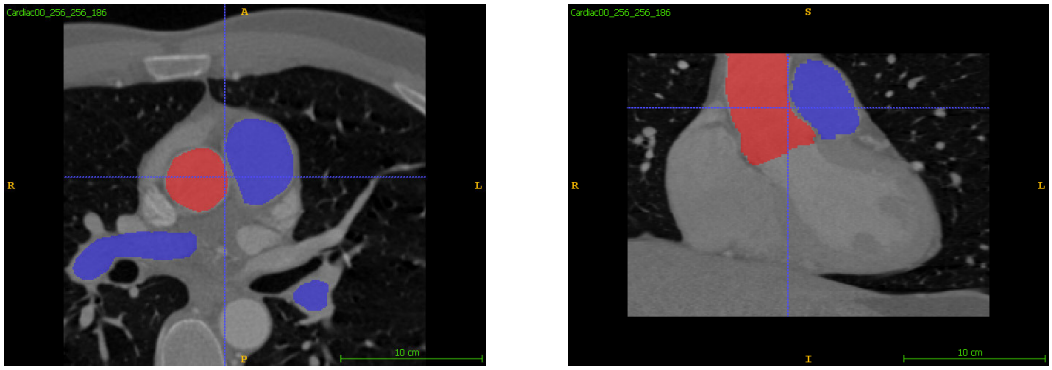

Figure 1: Axial view (left) and coronal view (right).

data visualization and segmentation for an axial slice and coronal slice can be seen in Figure 1. From ITK-SNAP, a stereolithography (STL) file was exported. This STL was translated, decimated, smoothed, and trimmed using Paraview and Meshmixer to better fit the hexahedral mesh of the ventricles. Since the vessel surfaces did not conform exactly to the ventricular outflow tracts, a loft was created between the top of the interior surface of the ventricle and the bottom of the vessel. Structure geometries were constructed from the STL files in SOLIDWORKS (Dassault Systemes SOLIDWORKS Corporation, Waltham, MA, USA). The loft and vessel were combined and exported as an ACIS file in ASCII (SAT) format. Volumes for the great vessels and valves were imported into Trelis (Computational Simulation Software, LLC, American Fork, UT, USA). Except for the mitral and tricuspid valve chordae, triangular meshes were created for the surfaces, from which a conforming tetrahedral mesh was created for the volumes. The chordae were meshed with a single strand of hexahedral elements.

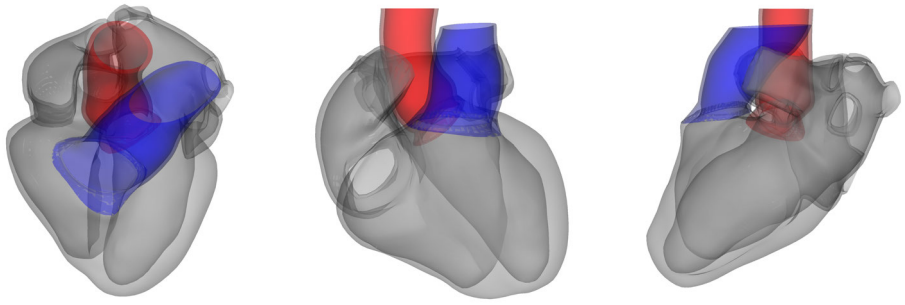

Figure 2: Heart geometry reconstructed from CT data.

Figure 2 displays the heart geometry in grey, with the pulmonary artery and aorta geometries in blue and red respectively. The geometries for the great vessels overlap with

the heart geometry by about 2 elements; from equation (5), the overlapping region moves with the same velocity, ensuring the great vessels do not come apart from their outflow tracts. Nothing further is done to glue these geometries together in our simulations.

Idealized models for the heart valves are displayed in Figure 3. The aortic and pulmonary valves were created by forming a single leaflet, uniformly thickening it, and rotating it about the valve axis. The mitral and tricuspid valve surfaces were designed from a parametrized superquadric surface described in [8]. We uniformly thickened this surface and trimmed it to define the different leaflets. These models include an idealized description of chordae and papillary muscles. The position of the papillary muscle was chosen to match the medical images. The valve models were registered with the heart geometry by transformations peformed in SOLIDWORKS. To prevent separation of the the structures in our simulations, all models intersect the heart and great vessel geometries.

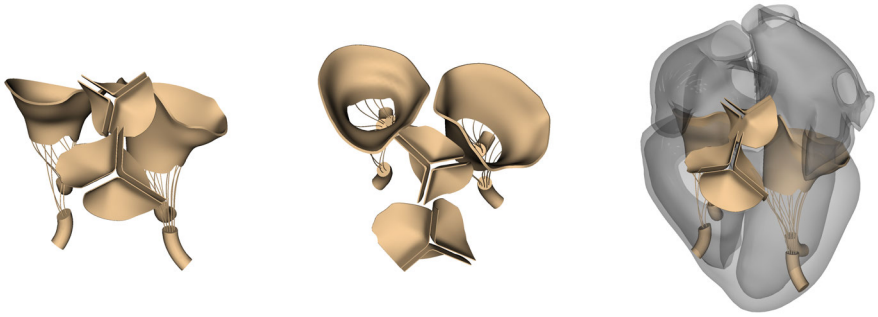

Figure 3: Idealized valve geometry.

5 CONSTITUTIVE MODELS AND BOUNDARY CONDITIONS

In these preliminary simulations, we use a neo–Hookean constitutive model for the valves, ascending aorta, and pulmonary artery. The strain energy functional takes the form:

$$W_{\text{nh}}(\mathbb{F}) = \frac{\mu_e}{2}\,(I_1 - 3)\,, \quad U(J) = \beta_s(J\log\,J - J + 1),$$

for some material parameter μ_e, where $I_1 = \text{tr}(\mathbb{F}\mathbb{F}^T)$, and some additional parameter β_s which determines the strength of the volumetric penalization. The corresponding first Piola-Kirchhoff stress is

$$\mathbb{P}^{\text{s}}_{\text{nh}} = \mu_e\left(\mathbb{F} - \frac{I_1}{3}\mathbb{F}^{-T}\right) + \beta_s J\log J\mathbb{F}^{-T}.$$

The contractile heart tissue is modeled as a fiber reinforced solid using the transversely isotropic constitutive model from Guccione et al. [6]. This formulation requires the specification of a fiber vector field $\boldsymbol{f}_0$ defined within the heart myocardium which qualitatively

aligns with the orientation of the cardiomyocytes. Given specified material parameters $b_{\text{f}}, b_{\text{t}}, b_{\text{fs}}$, and c, the strain energy functional for the passive myocardium is defined:

$$W_{\text{myo}}(\mathbb{F}) = \frac{c}{2}\left(e^{Q} - 1\right),$$
$$Q = b_{\text{f}}\tilde{E}_{11}^2 + b_{\text{t}}(\tilde{E}_{22}^2 + \tilde{E}_{33}^2 + \tilde{E}_{23}^2 + \tilde{E}_{32}^2) + b_{\text{fs}}(\tilde{E}_{12}^2 + \tilde{E}_{21}^2 + \tilde{E}_{13}^2 + \tilde{E}_{31}^2),$$

with $\tilde{E}_{ij}$ components of the Green–Lagrange strain tensor $\frac{1}{2}(\mathbb{F}^T\mathbb{F} - \boldsymbol{I})$ rotated so the first unit vector aligns with a specified fiber direction $\boldsymbol{f}_0$. Given a time periodic function $T(t)$ with period equal to a cardiac cycle, the active contractile part of the first Piola–Kirchoff stress is given as $T(t)\mathbb{F}\,\boldsymbol{f}_0 \times \boldsymbol{f}_0$. In sum, the total stress for the heart myocardium model is:

$$\mathbb{P}^{\text{s}}_{\text{myo}}(\boldsymbol{X}, t) = \text{DEV}\left[\frac{\partial W_{\text{myo}}}{\partial \mathbb{F}} + T(t)\mathbb{F}\,\boldsymbol{f}_0 \otimes \boldsymbol{f}_0\right] + \beta_s J \log(J)\mathbb{F}^{-T}.$$

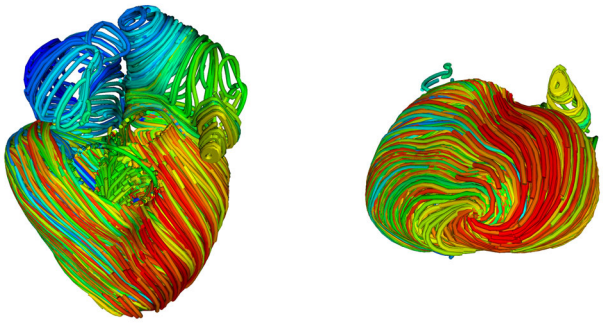

Figure 4: Visualization of the heart fiber vector field. The colors correspond to distinct seed points.

Figure 4 depicts a visualization of the fiber vector field by plotting streamlines; different colors correspond to distinct seed points. The fiber field is constructed by solving a collection of Poisson problems on the heart mesh, and using gradients of the resulting harmonic fields to define the local fiber orientation.

The heart is loosely held in place during our simulations through tether force boundary conditions and body forces. These conditions take the form of a linear restoring force depending on displacement from the reference configuration:

$$\boldsymbol{F}_{\text{tether}}(\boldsymbol{X}, t) = \kappa\left(\boldsymbol{\chi}(\boldsymbol{X}, t) - \boldsymbol{\chi}(\boldsymbol{X}, 0)\right),$$

with the parameter κ describing the tethering strength. We use this tethering as a body force on the vena cavas and pulmonary veins, and as a surface force on the top of the pulmonary artery and aorta. These conditions are built into the volumetric force density and projected onto the finite element basis via equation (6).

b_{f}	b_{t}	b_{fs}	c (kPa)	$T_{\max}$ (kPa)
4	1	2	2	1.2×10^2

Table 1: Parameters for the myocardium constitutive model.

6 RESULTS

In this section, we provide some results during early ventricular systole. Visualization of computational results is done using VisIt [3]. The active contraction function $T(t)$ for the left and right ventricles linearly increases from zero to its maximum value $T_{\max}$ over 0.4 seconds. Parameters for the myocardium constitutive model are given in Table 1.

Velocity streamline plots are shown in Figure 5, at 0.131 seconds on the left and 0.117 seconds on the right. The color bar indicates the magnitude of the velocity field in cm/s. Seed points were uniformly placed in spheres contained within the ventricles.

Figure 6 depicts displacement, with the color bar indicating magnitude of the displacement field $\boldsymbol{\chi}(\boldsymbol{X}, t) - \boldsymbol{\chi}(\boldsymbol{X}, 0)$ in cm. This slice highlights the dynamics on the left side of the heart; in particular, the aortic valve fully opens and the mitral valve closes.

Snapshots in time for the magnitude of the velocity field, on a slice of the Cartesian grid bisecting the aorta, are shown in Figure 7. This slice is superimposed with the heart model. Figure 8 displays analogous results for the pulmonary artery. One can see substantial flow through both of these great vessels.

Since the reference configurations for the aortic/pulmonary valves and the mitral/tricuspid valves are closed and open respectively, we also investigate valvular dynamics during ventricular contraction in Figures 9 and 10. In particular, during this part of the cardiac cycle the aortic/pulmonary valves open and the mitral/tricuspid valves close. Our simulations are able to capture these dynamics, as well as reveal that the pulmonic valve opens after the aortic valve.

7 DISCUSSION

Our future work includes the construction of more realistic fiber reinforced constitutive models for the valves, and the inclusion of pericardial boundary conditions and proper loading conditions for the fluid. These enhancements will enable a baseline model for the human heart, from which we hope to computationally investigate various clinical interventions and medical devices.

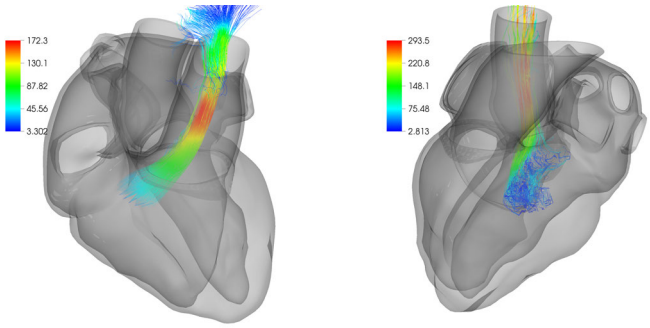

Figure 5: Velocity streamlines for the right ventricle on the left and the left ventricle on the right.

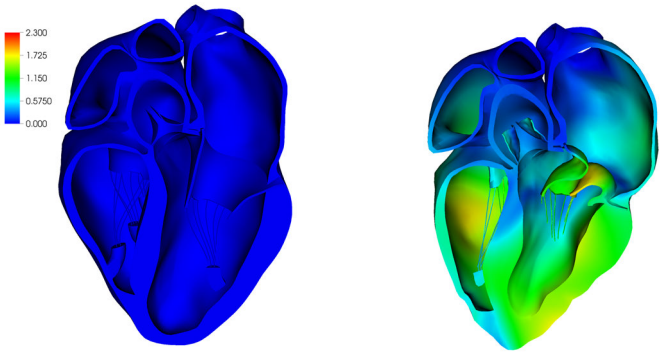

Figure 6: The color indicated the magnitude of the displacement field. On the left is the reference configuration and on the right is a snapshot at time 0.132 seconds.

REFERENCES

[1] Brian Baillargeon, Nuno Rebelo, David D Fox, Robert L Taylor, and Ellen Kuhl. The living heart project: a robust and integrative simulator for human heart function. *European Journal of Mechanics-A/Solids*, 48:38–47, 2014.

[2] Daniele Boffi, Lucia Gastaldi, Luca Heltai, and Charles S Peskin. On the hyper-elastic formulation of the immersed boundary method. *Computer Methods in Applied Mechanics and Engineering*, 197(25-28):2210–2231, 2008.

[3] Hank Childs, Eric Brugger, Brad Whitlock, Jeremy Meredith, Sean Ahern, David Pugmire, Kathleen Biagas, Mark Miller, Cyrus Harrison, Gunther H. Weber, Hari Krishnan, Thomas Fogal, Allen Sanderson, Christoph Garth, E. Wes Bethel, David Camp, Oliver Rübel, Marc Durant, Jean M. Favre, and Paul Navrátil. VisIt: An End-User Tool For Visualizing and Analyzing Very Large Data. In *High Performance Visualization–Enabling Extreme-Scale Scientific Insight*, pages 357–372. Oct 2012.

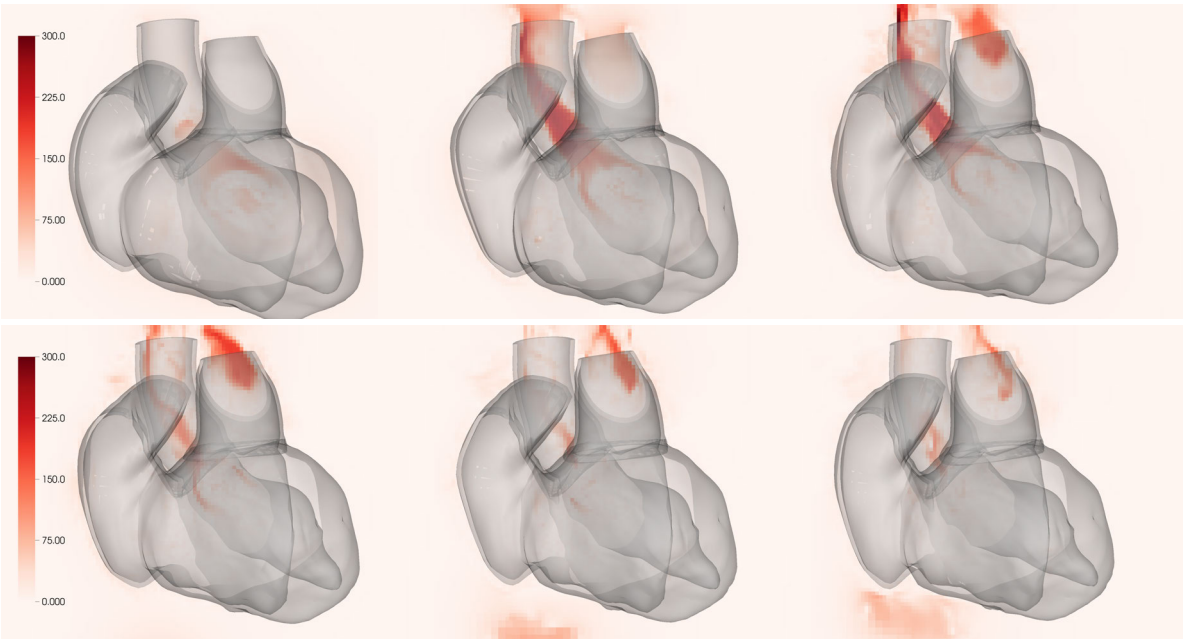

Figure 7: Magnitude of fluid velocity through ascending aorta from 0.049 seconds to 0.293 seconds incrementing by approximately 0.049 seconds in each frame across the top, then across the bottom.

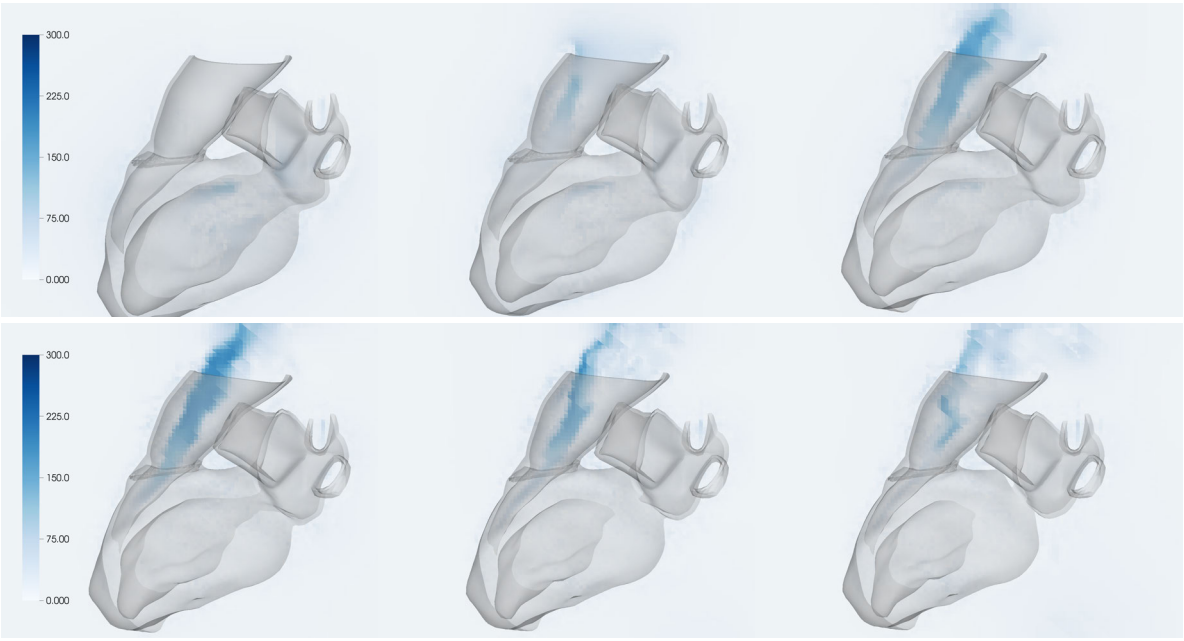

Figure 8: Magnitude of fluid velocity through ascending pulmonary artery from 0.049 seconds to 0.293 seconds incrementing by approximately 0.049 seconds in each frame across the top, then across the bottom.

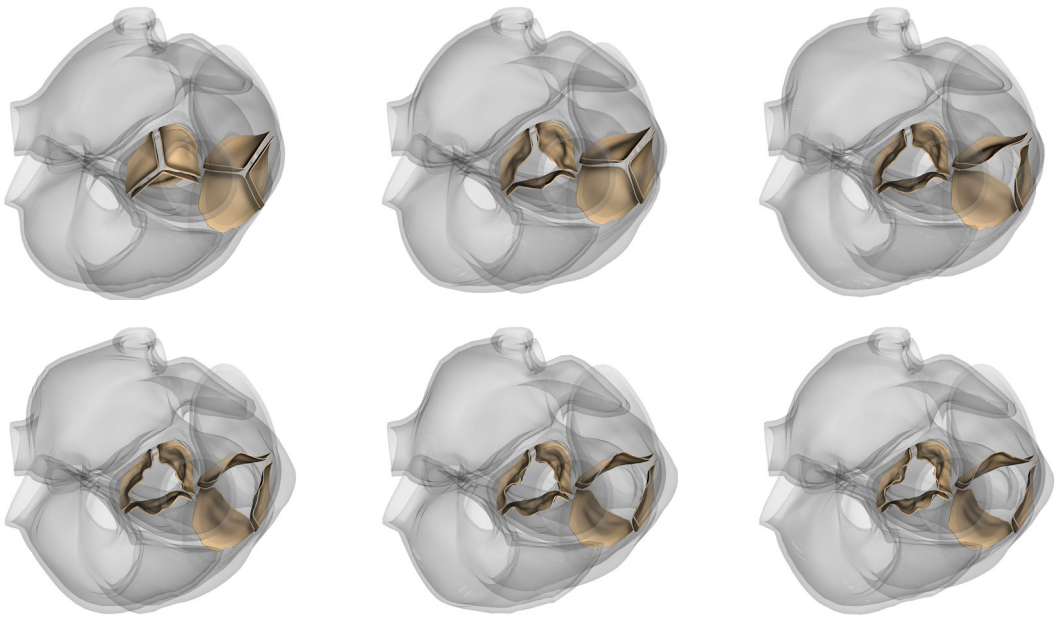

Figure 9: Idealized aortic and pulmonic valves opening from 0.029 seconds to 0.176 seconds incrementing by approximately 0.029 seconds in each frame across the top, then across the bottom.

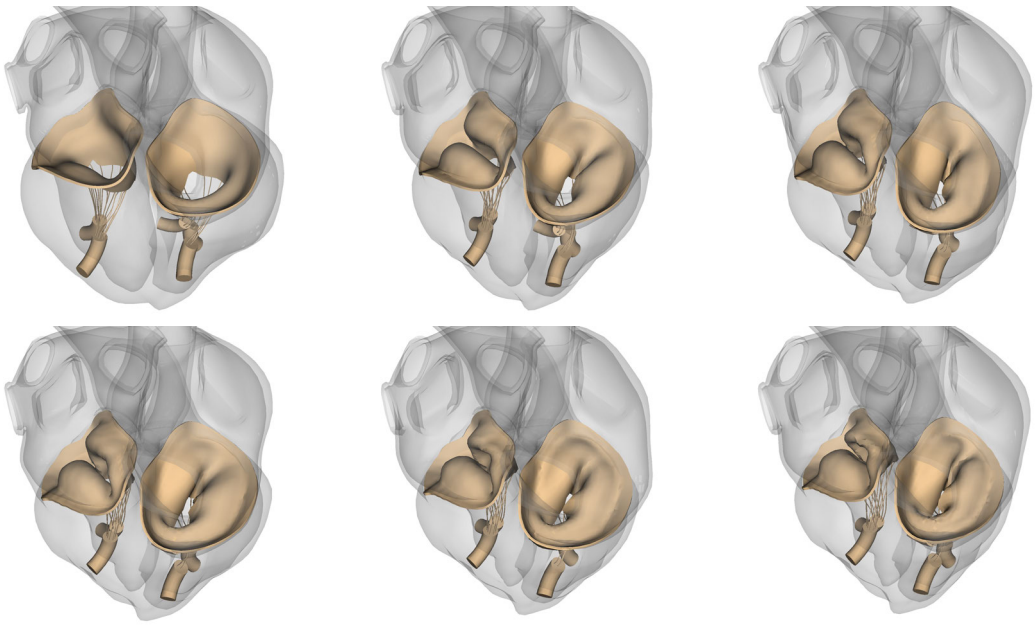

Figure 10: Idealized mitral and tricuspid valves opening from 0.029 seconds to 0.176 seconds incrementing by approximately 0.029 seconds in each frame across the top, then across the bottom.

[4] Boyce E Griffith and Xiaoyu Luo. Hybrid finite difference/finite element immersed boundary method. *International Journal for Numerical Methods in Biomedical Engineering*, 33(12), 2017.

[5] Hao Gao, Liuyang Feng, Nan Qi, Colin Berry, Boyce E Griffith, and Xiaoyu Luo. A coupled mitral valveleft ventricle model with fluid–structure interaction. *Medical Engineering and Physics*, 47:128–136, 2017.

[6] Julius M Guccione, Kevin D Costa, and Andrew D McCulloch. Finite element stress analysis of left ventricular mechanics in the beating dog heart. *Journal of Biomechanics*, 28(10):1167–1177, 1995.

[7] Marc Hirschvogel, Marina Bassilious, Lasse Jagschies, Stephen M Wildhirt, and Michael W Gee. A monolithic 3d-0d coupled closed-loop model of the heart and the vascular system: Experiment-based parameter estimation for patient-specific cardiac mechanics. *International Journal for Numerical Methods in Biomedical Engineering*, 33(8), 2017.

[8] Amir H Khalighi, Andrew Drach, Robert C Gorman, Joseph H Gorman, and Michael S Sacks. Multi-resolution geometric modeling of the mitral heart valve leaflets. *Biomechanics and Modeling in Mechanobiology*, 17:351–366, 2018.

[9] David M McQueen and Charles S Peskin. A three-dimensional computer model of the human heart for studying cardiac fluid dynamics. *ACM SIGGRAPH Computer Graphics*, 34(1):56–60, 2000.

[10] DM McQueen, T O'Donnell, BE Griffith, and CS Peskin. Constructing a patient-specific model heart from CT data. In *Handbook of Biomedical Imaging*, pages 183–197. Springer, 2015.

[11] Alfio Quarteroni, Toni Lassila, Simone Rossi, and Ricardo Ruiz-Baier. Integrated heart – coupling multiscale and multiphysics models for the simulation of the cardiac function. *Computer Methods in Applied Mechanics and Engineering*, 314:345–407, 2017.

[12] Seiryo Sugiura, Takumi Washio, Asuka Hatano, Junichi Okada, Hiroshi Watanabe, and Toshiaki Hisada. Multi-scale simulations of cardiac electrophysiology and mechanics using the university of tokyo heart simulator. *Progress in Biophysics and Molecular Biology*, 110(2-3):380–389, 2012.

[13] Takumi Washio, Jun-ichi Okada, Akihito Takahashi, Kazunori Yoneda, Yoshimasa Kadooka, Seiryo Sugiura, and Toshiaki Hisada. Multiscale heart simulation with cooperative stochastic cross-bridge dynamics and cellular structures. *Multiscale Modeling & Simulation*, 11(4):965–999, 2013.